Cement & Concrete Composites 48 (2014) 42–52

Contents lists available at ScienceDirect

Cement & Concrete Composites

journal homepage: www.elsevier.com/locate/cemconcomp

Simulation of single fiber pullout response with account of fiber morphology

B.D. Ellis [a,*], D.L. McDowell [a,b], M. Zhou [a,b]

[a] Woodruff School of Mechanical Engineering, Georgia Institute of Technology, Atlanta, GA 30332-0405, USA
[b] School of Materials Science and Engineering, Georgia Institute of Technology, Atlanta, GA 30332-0405, USA

ARTICLE INFO

Article history:
Received 2 January 2012
Received in revised form 2 January 2014
Accepted 9 January 2014
Available online 19 January 2014

Keywords:
Cementitious composites
Fiber morphology
Finite element analysis
Twisted fibers

ABSTRACT

A finite element model was developed at the single fiber length scale to predict the quasi-static pullout response of individual fibers from cementitious composites. The model accounts for energy dissipation through granular flow of the interfacial transition zone (ITZ) and matrix, plastic work in the fiber, and frictional dissipation at the fiber–ITZ interface. The considered fiber morphology was a triangular cross section that had been uniformly twisted along the fiber length. The model was calibrated to published experimental data for fiber pitches of 12.7 and 38.1 mm/revolution pulled from cement mortar with a 44-MPa unconfined compressive strength. The model was used to investigate slip-hardening behavior, tunneling of the cement mortar, in situ pullout behavior of helically twisted fibers at a crack plane, and provide an alternate explanation for the pullout response of twisted fibers from a 84-MPa unconfined compressive strength matrix containing silica fume. Calculations show that twisted fibers can provide up to 5 times the peak pullout force and 10 times the total work compared with straight fibers and infer work-hardening behavior during fiber pullout. The findings indicate that the tailoring of fiber morphology and control of constituent properties are important avenues for achieving significant improvements in the performance of fiber-reinforced cementitious composites.

1. Introduction

The granular nature of concrete elicits a characteristic quasi-brittle behavior in tension. This undesirable behavior is often mitigated by embedding steel rebar within concrete; however, steel rebar within concrete presents new problems. For example, steel rebar reinforcement is relatively labor intensive to install, susceptible to corrosion through chloride ion transport, and unable to arrest cracks prior to the crack intersecting the steel rebar. Furthermore, the performance of rebar reinforced composites is highly susceptible to the placement of the rebar within the composite. An alternate reinforcement approach is to replace steel rebar with short, discontinuous fibers, resulting in Fiber Reinforced Cementitious Composites (FRCCs). Although they exhibit ductility and toughness [1], FRCCs' limitations in tensile loading require further investigation.

The tensile response of FRCCs depends on six factors: fiber volume fraction, fiber orientation, fiber shape, fiber material properties, cementitious material properties, and properties at the fiber–matrix interface. For steel fibers, it is desired to reduce the fiber volume fraction due to the relative expense of steel fibers compared to the cementitious matrix. Furthermore, fiber volume fractions greater than 2–4%, depending on the fiber's length to diameter ratio, may introduce porosity and fiber clumping during mixing [2]. Assuming a random orientation for short discontinuous fibers within a structure, the other four factors provide avenues for improving the tensile response of FRCCs.

Tensile responses of FRCCs at the mesoscale have been characterized by either direct tension tests of dog bone specimens (cf. Kim et al. [3]) or the flexural bending tests, defined by the American Society for Testing and Materials (ASTM) C1609 testing standard [4]. Both tests allow researchers to infer structure–property–performance relations of FRCCs by systematically changing the structure and material properties of the constituents. For example, Kim et al. [3] reported that FRCCs containing a 2% volume fraction of twisted fibers, defined as a fiber with a polygonal cross section that has been twisted along its primary axis, had between 25% and 49% greater mean first cracking strengths in direct tension tests than FRCCs containing 2% hooked fibers for matrices with unconfined compressive strengths between 28 and 84 MPa. Results for flexural bending tests indicate similar dependencies on the shape of the fiber. For example, Kim et al. [5] showed that FRCCs containing 1.2% fiber volume fractions of twisted fibers had a

* Corresponding author.
E-mail address: bellis7@gatech.edu (B.D. Ellis).

http://dx.doi.org/10.1016/j.cemconcomp.2014.01.003
0958-9465/

Nomenclature

$\underset{\sim}{\alpha}$	back stress tensor
$\underset{\sim}{\alpha}^{dev}$	deviatoric back stress tensor
A_f	cross-sectional area of fiber
β	internal friction angle
β_i	internal friction angle – ITZ
β_m	internal friction angle – matrix
c	constant
C	material constant - fiber
d	cohesion under pure shear
φ_e	equivalent fiber diameter
D^p	plastic part of the rate of deformation tensor
$\tilde{\varepsilon}^{pl}$	equivalent plastic strain – fiber
$\underset{\sim}{\dot{\varepsilon}}^{pl}$	plastic strain tensor
$\dot{\tilde{\varepsilon}}^{pl}$	equivalent plastic strain rate – fiber
$\dot{\varepsilon}^p$	equivalent plastic strain rate
E_i	elastic stiffness – ITZ
E_f	elastic stiffness – fiber
E_m	elastic stiffness – matrix
F	yield condition
$\underset{\sim}{F}$	deformation gradient tensor
$\underset{\sim}{F}^e$	elastic deformation gradient tensor
$\underset{\sim}{F}^n$	inelastic deformation gradient tensor
$\tilde{f}_i$	unconfined compressive strength – ITZ
f_m	unconfined compressive strength – matrix
G	flow potential
γ	material parameter – fiber
$\dot{\gamma}_i$	shearing rate ($i = 1, 2$)
ITZ	interfacial transition zone
I	2nd rank identity tensor
$\underset{\sim}{K}$	ratio of yield stress in triaxial tension to yield stress in triaxial compression
K_i	ratio of yield stress in triaxial tension to yield stress in triaxial compression – ITZ
K_m	ratio of yield stress in triaxial tension to yield stress in triaxial compression – matrix
$\dot{\lambda}$	plastic multiplier
L_e	fiber embedded length
L_{free}	fiber free length
ν_i	Poisson's ratio – ITZ
ν_f	Poisson's ratio – fiber
ν_m	Poisson's ratio – matrix
μ	coefficient of coulomb friction
p	hydrostatic pressure
$p_{contact}$	contact pressure at interface
q	mises equivalent stress
ρ_i	mass density – ITZ
ρ_f	Mass density - fiber
ρ_m	mass density – matrix
r	third invariant of deviatoric stress
σ^o	yield stress – fiber
$\underset{\sim}{\sigma}$	cauchy stress tensor
$\underset{\sim}{S}$	deviatoric stress
$\underset{\sim}{\tau}_{eq}$	equivalent frictional stress
τ_i	shear stress at interface between two different materials ($i = 1, 2$)
τ_{crit}	critical frictional stress
t	extended Drucker–Prager stress in meriodonal plane
$\underset{\sim}{u}$	displacement vector
$\underset{\sim}{x}$	deformed coordinate system
$\underset{\sim}{X}$	fixed reference coordinate system
$\tilde{\psi}_i$	dilation angle – ITZ
ψ_m	dilation angle – matrix

13% greater mean modulus of rupture than FRCCs containing hooked fibers. Flexural bending tests reported by Soroushian and Bayasi [6] reported that FRCCs containing 2% volume fraction straight smooth fiber had a 35% reduction in modulus of rupture as compared to FRCCs containing 2% volume fraction off hooked fibers with a similar length and diameter. Clearly, the geometry of a fiber influences the tensile properties of FRCCs.

To understand why one fiber geometry is more effective than another, single fiber pullout tests are used to characterize the pullout responses of fibers with different morphologies. As reported by many researchers (e.g., Easley et al. [7]; Kim et al. [3]; Boshoff et al. [8]; Cunha et al. [9]), a single straight, smooth fiber pulled in the axial direction from a cementitious matrix exhibits three common energy storage and dissipation stages: (1) an initial elastic storage stage, in which the fiber undergoes relatively small displacements before the peak force is reached; (2) a debonding stage, in which the chemical bonds between the fiber and cementitious matrix break, resulting in a drop in force; and (3) a friction-dominated stage, in which the pullout force decreases monotonically as the fiber pulls out. For straight, smooth fibers, the fiber length has a strong influence on the peak pullout force. For example, Cunha, Barros, and Sena-Cruz [9] reported a 100% increase in peak pullout force when fiber length is increased from 20 mm to 30 mm. Additional studies were conducted by Chan and Chu [10] and Guerrero and Naaman [11] to determine the effects of matrix constituents on pullout behavior.

Analytical models of a single straight, smooth fiber being pulled out of a matrix have been framed in terms of energy balance [12] and equilibrium [13]. The equilibrium-derived analytical model uses experimental data to determine five constants: bond modulus, bond strength, constant frictional bond stress, and two decaying frictional parameters. Numerically, Li and Mobasher [14] used a two-dimensional axisymmetric framework containing three linear elastic constitutive relations to simulate the three pertinent materials: fiber, interface, and matrix. The modeled mechanisms include fiber debonding and friction. A clamping pressure was applied at the outer edge of the matrix to simulate shrinkage. Results were presented and compared to experimental data for the first 0.1 mm of end slip.

Hooked fibers exhibit behaviors different from those of straight fibers. As reported by Cunha et al. [9], a hooked fiber embedded 20 mm into a matrix shows a peak pullout force approximately 4.5 times that of a straight, smooth fiber embedded at the same depth. Even though the peak pullout force of a hooked fiber increases with the embedded length of the fiber, the increase is not as pronounced as that for straight, smooth fibers [9]. In addition to the three energy storage and dissipation mechanisms of straight, smooth fibers, hooked fibers also dissipate energy via plastic work during pullout. Although not a distinct mechanism, the residual stress at a fiber's hook appears to increase normal tractions and ultimately the force required during the friction-dominated stage of pullout.

An analytical model to predict the pullout force versus end slip relation for hooked fibers was introduced by Alwan et al. [15], who extended the model of straight, smooth fibers given by Naaman et al. [13]. The model predicts four different characteristic

responses depending on the end slip of the fiber. The first characteristic response is a rapid increase in pullout load as the fiber undergoes debonding. Second, the pullout force increases to a maximum value and maintains the maximum value as both kinks in the embedded end of the fiber respond as plastic hinges during increased end slip. The third characteristic response occurs after the furthest embedded kink of the hooked fiber completely passes through the furthest kink of the fiber bed. At this point, the pullout force decreases to a lower value until the fiber is completely removed from the hooked part of the fiber bed, thus leading to the characteristic fourth response: a friction dominated pullout similar to a straight, smooth fiber.

Twisted fibers display behavior that is different from that of either straight, smooth fibers or hooked fibers. The single fiber pullout results in Naaman [16] indicate substantial differences in end slip at maximum pullout force, maximum pullout force, and pullout forces for end slips greater than the end slip at the maximum pullout force. During pullout, twisted fibers generate maximum pullout forces at end slips of 20–40% of the fiber's embedded length, whereas hooked and straight, smooth fibers reach maximum pullout forces at end slips of approximately 10% and less than 1% of the fiber embedded length, respectively. The work-hardening behavior displayed by twisted fibers has important implications for the distribution of damage throughout structural-level length scales [17]. The second difference is that twisted fibers generate peak pullout forces on the order of three to five times those of straight, smooth fibers, depending on the morphology of the twisted fiber. The third difference is that twisted fibers maintain pullout forces close to the maximum pullout force for up to 80% of a fiber's embedded length. These three differences cause the total work for pullout of a twisted fiber to be eight to ten times greater than that for a straight, smooth fiber [16]. Other studies concerning twisted fibers have determined the influence of matrix composition [11], the rate of pullout [3], and the number of fiber strands [18]. Although Naaman and coworkers were first to use twisted, polygonal, discontinuous, and randomly oriented fibers, Menzel [19] documented similar improvement in the pullout behavior of continuous steel rebar reinforcement placed in cementitious matrices. Menzel's results indicate that a helically threaded rebar reinforcement sustains greater than 10 times the stress of a straight, smooth rebar over the first 0.40 mm of end slip.

An analytical model to predict the pullout of a twisted fiber was presented by Sujivorakul and Naaman [20], with complete details given by Sujivorakul [21]. The analytical model assumes a homogeneous elastic matrix surrounding an elastic–plastic fiber. The model accounts for the fiber's embedded length, cross-sectional shape, pitch, untwisting torque, tensile strength of the fiber, and friction between the fiber and the matrix. Calibration of the model requires experimental data pertaining to the bond shear stress versus slip relation, untwisting torque at the embedded tip of the fiber, and a locking torque coefficient, each of which depend upon the pitch of the fiber and the cementitious matrix surrounding the fiber. In other words, for a given fiber and matrix, a different calibration is required for each pitch and matrix. Although the analytical model has been used to predict the pullout force during the first 5 mm of end slip, the model does not capture the experimentally observed matrix tunneling, defined as the erosion of the matrix surrounding the fiber as the fiber is pulled from the matrix, or the resulting rapid decrease in pullout force at end slips between 70% and 80% of the fiber's initial embedded length.

The primary objective of this research is to investigate the mechanisms active during the pullout of a single twisted fiber from a cementitious composite. To achieve this objective, this research introduces a numerical model at the single fiber length scale accounting for fiber morphology as well as three phases of material: fiber, an interfacial transition zone (ITZ) between the fiber and the surrounding matrix, and the matrix. The dissipation mechanisms considered include plastic deformation of the fiber, friction at the fiber–ITZ interface, and plastic deformation due to granular flow, i.e., plastic deformation of granular materials, of the ITZ and matrix. The numeric model provides insights into the active physical mechanisms not possible by physical experiments or analytical models; thus, it is intended that this model will provide a means for improving the design of twisted fibers in the future.

2. Framework of analysis and constitutive models

The numerical model considers finite deformation. A material point initially at a fixed reference coordinate X moves to a deformed coordinate x. The mapping between x and X is specified by the displacement vector. The deformation gradient is defined by $F = \frac{\partial x}{\partial X}$. For elastic–plastic materials, the deformation gradient is multiplicatively decomposed via $F = F^e \cdot F^n$ where F^e and F^n are the elastic and inelastic deformation gradients, respectively. The deviatoric stress S is defined by $S = \sigma + p\,I$, where σ, p, and I are the Cauchy stress tensor, the hydrostatic pressure, and the second rank identity tensor, respectively. The pressure is given by $p = -\frac{1}{3}\,\sigma : I$.

2.1. Constitutive relations – matrix

The matrix is represented by a pressure sensitive and strain-rate insensitive extended Drucker–Prager constitutive relation included as part of Abaqus/Explicit v6.10 [22]. The extended Drucker–Prager constitutive relation assumes the yield condition

$$F = t - p\tan(\beta) - d \leqslant 0, \tag{1}$$

where

$$t = \frac{1}{2}q\left[1 + \frac{1}{K} - \left(1 - \frac{1}{K}\right)\left(\frac{r}{q}\right)^3\right]. \tag{2}$$

Here, β is the internal friction angle in the meridional stress plane, and d is the cohesion of the material under pure shear. In Eq. (2), q is the Mises equivalent stress defined by $q = \sqrt{\frac{3}{2}(S : S)}$, K is the ratio between the yield stress in triaxial tension and the yield stress in triaxial compression and must be in the range $0.778 \leqslant K \leqslant 1.0$, and r is the third invariant of the deviatoric stress defined by $r = (\frac{9}{2}\,S \cdot S : S)^{\frac{1}{3}}$. Setting $K = 1$ allows the original Drucker–Prager [23] yield condition to be recovered due to the lack of dependence on the third invariant of deviatoric stress. The von Mises yield condition is recovered when $K = 1$ and $\beta = 0$.

When the yield condition is satisfied (i.e., $F = 0$), a non-associative material yields according to the flow rule

$$D^p = \frac{\dot{\varepsilon}^p}{c}\frac{\partial G}{\partial \sigma}, \tag{3}$$

where D^p is the plastic part of the rate of deformation tensor, $\dot{\varepsilon}^p$ is the equivalent plastic strain rate defined by $\dot{\varepsilon} = \sqrt{\frac{2}{3}D^p : D^p}$, c is a constant defined by $c = 1 - \frac{1}{3}\tan(\psi)$, G is the flow potential

$$G = t - p\tan(\psi), \tag{4}$$

and ψ is the dilation angle.

In this paper, we consider normal weight cementitious matrix with a mass density, ρ_m, of 2.4 g/cm^3 and unconfined compressive strengths, f_m, of 44 and 84 MPa. The elastic stiffness of the cementitious matrix, E_m, is calculated using the empirical relation

$$E_m = 2.15 \times 10^4 \left(\frac{f_m}{10}\right)^{1/3} \tag{5}$$

where f_c is specified in MPa. Eq. (5) is from CEP-FIP Model 1990 [24], which is valid for normal weight concrete containing quartz

aggregate and 28-day unconfined compressive strengths less than 80 MPa [25]. For $f_m = 44$ MPa and 84 MPa, the calculated elastic stiffness values are 35.2 and 43.7 GPa, respectively. Possible softening of the matrix during large deformations is not considered.

The ratio of the yield stress in triaxial tension to the yield stress in triaxial compression and the internal friction angle are assumed to be $K_m = 0.8$ and $\beta_m = 28°$, as determined by Park et al. [26]. The dilation angle, ψ_m, is used as a calibration coefficient to fit the model to experimental data presented in Sujivorakul [21]. The choice of possible dilation angles is guided by Vermeer and dr Borst [27], who showed that the $\psi < \beta$ in all cases and observed that the dilation angles of concrete are between 0 and 20. From the calibration, the dilation angle of the cementitious matrix is set to a constant value of 2°. Table 1 summarizes the material parameters used for the two different cementitious matrices considered.

2.2. Constitutive relations – interfacial transition zone (ITZ)

The constitutive relations for the ITZ follow those of the cementitious matrix described in Section 2.1 except that elastic stiffness of the ITZ, E_i, and the dilation angle of the ITZ, ψ_i, are reduced. The choice of E_i is guided by Cohen et al. [28], who estimated E_i/E_m as a function of ITZ thickness using the logarithmic rule of mixtures. For an assumed ITZ thickness of 50 μm, Cohen, Lee, and Goldman estimated E_i/E_m to be 0.75 for Portland Cement mortars and 0.88 for a cementitious matrix where 10% of the Portland Cement has been replaced with silica fume. Here, E_i/E_m is assumed to be a constant value of 0.8.

The dilation angle in the ITZ is used as a calibration constant and assumed to have a more restrictive upper bound, namely $\psi_i \leqslant \psi_m$. Calibration of the model indicates that $\psi_i = 1$.

2.3. Constitutive relations – fiber

The fiber is assumed to be an elastic–plastic pressure- and rate-independent material. Yielding of the fiber is assumed to follow the Von Mises yield criterion in the form of

$$F(\underset{\sim}{\sigma}, \underset{\sim}{\alpha}, \sigma^o) = \sqrt{\frac{3}{2}\left(\underset{\sim}{S} - \underset{\sim}{\alpha}^{dev}\right) : \left(\underset{\sim}{S} - \underset{\sim}{\alpha}^{dev}\right)} - \sigma^o = 0, \tag{6}$$

where S is the previously defined deviatoric stress tensor, $\underset{\sim}{a}$ is the backstress tensor, $\underset{\sim}{a}^{dev}$ is the deviatoric part of the backstress tensor defined as $s^{dev} = \underset{\sim}{a} - \frac{1}{3}\, a : I$, and σ^o is the yield stress. The yield surface evolves through the evolution of the backstress tensor, i.e.,

$$\dot{\underset{\sim}{\alpha}} = \frac{C}{\sigma^o}(\underset{\sim}{\sigma} - \underset{\sim}{\alpha})\dot{\bar{\varepsilon}}^{pl} - \gamma\, \underset{\sim}{\alpha}\, \dot{\bar{\varepsilon}}^{pl} \tag{7}$$

where C and γ are material parameters and $\dot{\bar{\varepsilon}}^{pl}$ is the equivalent plastic strain rate defined as $\dot{\bar{\varepsilon}}^{pl} = \sqrt{\frac{2}{3}\dot{\underset{\sim}{\varepsilon}}^{pl} : \dot{\underset{\sim}{\varepsilon}}^{pl}}$. Because the inelastic flow is assumed to be associative, the evolution equation for plastic strain is

$$\dot{\underset{\sim}{\varepsilon}}^{pl} = \dot{\lambda}\frac{\partial F}{\partial \underset{\sim}{\sigma}}, \tag{8}$$

where $\dot{\lambda}$ is the plastic multiplier obtained from the consistency condition $dF = 0$. Damage initiation and damage evolution are not considered.

The fiber's density, ρ_f, elastic stiffness, E_f, and Poisson's ratio, v_f, are assumed to be 7.85 g/cm^3, 190 GPa, and 0.33. The remaining material parameters were determined from monotonic uniaxial tensile data of a non-twisted triangular fiber reported in Sujivorakul [21]. The triangular fiber was manufactured by shaping music wire, initially with a round cross section and confirming to ASTM A228 [29]. The triangular shape was approximately the shape of an isosceles triangle with an equivalent diameter, ϕ_e, of 0.5 mm. Here, the equivalent diameter is defined as $\phi_e = 2\sqrt{A_f/\pi}$, where A_f is the cross-sectional area of the triangular fiber.

Fig. 1 compares the engineering stress as a function of engineering strain for experimental data and numerical simulations of a uniaxial monotonically loaded triangular shaped fiber which was not twisted prior to testing. In Fig. 1, the solid black line represents the experimentally observed behavior presented by Sujivorakul [21]; the dashed red line represents the engineering stress-engineering strain behavior of numerical simulations. The calibration constants were determined to be $\sigma^o = 1.15$ GPa, $C = 260$ GPa, and $\gamma = 195$ via simulation of a 25.4-mm long non-twisted fiber with a triangular cross section.

2.4. Constitutive relations – interfacial friction

The friction model used is the rate-independent, isotropic Coulomb friction law. In this model, relative motion between two surfaces is allowed when the equivalent shear stress

$$\tau_{eq} = \sqrt{\tau_1^2 + \tau_2^2} \tag{9}$$

reaches or exceeds the critical stress

$$\tau_{crit} = \mu p_{contact}, \tag{10}$$

where τ_1 and τ_2 are mutually orthogonal shear stresses at the interface, μ is the coefficient of friction, and $p_{contact}$ is the normal contact pressure between the two surfaces. Because the model is assumed to be isotropic, the magnitudes of the shearing rates

$$\begin{aligned} \dot{\gamma}_1 &= \sqrt{\dot{\gamma}_1^2 + \dot{\gamma}_2^2}\,\frac{\tau_1}{\tau_{eq}} \text{ and} \\ \dot{\gamma}_2 &= \sqrt{\dot{\gamma}_1^2 + \dot{\gamma}_2^2}\,\frac{\tau_2}{\tau_{eq}} \end{aligned} \tag{11}$$

are proportional to the shear stresses τ_1 and τ_2.

The coefficient of Coulomb friction is determined from the experiments of Baltay and Gjelsvik [30], who found that the coefficient of friction between steel and concrete depends on the surface finish of the steel. For machined steel surfaces, the mean coefficient of friction was measured over the range of normal pressures from 13.8 kPa to 55 MPa. Although Baltay and Gjelsvik [30] assigned a mean value of 0.47, the data for machined steel surfaces indicate a parabolic response with the maximum value of $\mu = 0.58$

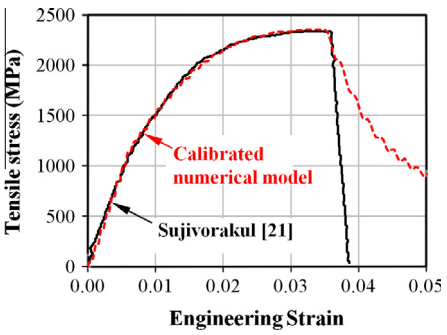

Fig. 1. Comparison of experimental (solid black) and simulation (dashed red) stress–strain data for monotonically loaded tensile specimens. The fibers have cross sections in the shape of an isosceles triangle with $\varphi_e = 0.5$ mm. (For interpretation of the references to colour in this figure legend, the reader is referred to the web version of this article.)

Table 1
Material parameters used for cementitious matrix.

f_m (MPa)	ρ_m (g/cm^3)	E_m (GPa)	K_m ( )	β_m (°)	ψ_m (°)
44	2.4	35.2	0.8	28	2

for a normal stress of 3.4 MPa and a minimum value of $\mu = 0.35$ for $p_{contact} \leqslant 3.4$ MPa and $p_{contact} \geqslant 55$ MPa. For steel surfaces with mill scale, Baltay and Gjelsvik [30] reported that the coefficient of friction is 0.2 for $p_{contact} = 10$ kPa and increases to 0.53 for $p_{contact} = 34.5$ MPa. In this work, a pressure-independent coefficient is assumed to be 0.45 at steel-ITZ interfaces.

For cementitious materials in contact with other cementitious materials, the American Concrete Institute ACI 381 [31] recommends higher pressure-independent coefficients of friction, namely 1.0 for normal-weight concrete placed against another hardened concrete with an intentionally roughened surface, and 1.4 for cementitious surfaces formed within a monolithically placed structure. In this work, a pressure-independent coefficient is assumed to be 1.05 at interfaces formed as a result of fracture within cementitious materials.

3. Model description

The model at the single fiber length scale is implemented in three dimensions with a single fiber embedded in a 50-μm-thick ITZ, which is then embedded within a cementitious matrix. Fig. 2 shows a sample instantiation of the reference configuration of the model with the matrix shaded gray, ITZ shaded red, and fiber shaded green. In Fig. 2, the triangular fiber has an $\varphi_e = 0.5$ mm, a 12.7-mm pitch, and a total length of 15.5 mm, of which 12.5 mm has been embedded into the matrix. The remaining 3 mm is classified as the free length, L_{free}, of the fiber. The numbers 1–6 in yellow rectangles define faces of the model for future reference. Relative displacements between the nodes on the external surface of the fiber and the nodes on the internal surface of the ITZ are permitted; however, relative displacements between the nodes on the external surface of the ITZ and the nodes on the internal surface of the matrix are not permitted.

The geometric scale of the model resolves fiber cross-sectional shape, fiber length, and helical pitch along the fiber's axis. All fibers have cross sections in the shape of isosceles triangles with $\varphi_e = 0.5$ mm. The model assumes perfect geometrical contact at the fiber–ITZ and ITZ–matrix interfaces (i.e., no voids) and pressure-independent dilation angles in the matrix and the ITZ. Fiber warping and residual stresses caused by twisting of non-circular prismatic fibers [32], as well as chemical adhesion between the fiber and the ITZ are disregarded.

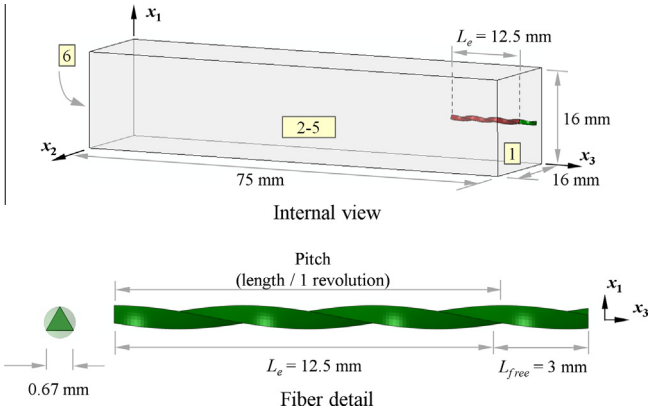

Fig. 2. Illustration of the model's internal view showing the matrix (gray), ITZ (red), and fiber (green). The fiber shown in the fiber detail view has a $\varphi_e = 0.5$ mm triangular cross-section, 12.7-mm pitch, and a 15.5-mm total length, of which 12.5 mm is embedded into the cementitious material. (For interpretation of the references to colour in this figure legend, the reader is referred to the web version of this article.)

3.1. Boundary and loading conditions

The boundary conditions are applied in two steps. In the first step, face 1 of the fiber is fixed in the x_3 direction while the matrix and ITZ domains undergo an isotropic volume shrinkage in accordance with recommendations of CEB-FIB Model Code 1990 [24]. For a normal hardening cement with a $f_c = 44$ MPa, CEB-FIB recommends a linear shrinkage of −280 μm/m after 2 days of curing. The linear shrinkage is applied via a smooth step function prebuilt in Abaqus such that the linear shrinkage is 0 μm/m at 0 ms, −280 μm/m at 0.008 ms, and the partial derivative of shrinkage with respect to time is zero at 0 and 0.008 ms. Rigid body translation is prevented by fixing the center point of the fiber's positive x_3 face in the x_1 and x_2 directions.

In the second step, the fiber is pulled from the ITZ and matrix. Matrix faces 1–5 are traction-free; face 6 of the matrix is fixed in the x_1, x_2, and x_3 directions. Face 1 of the fiber is pulled in the x_3 direction at a velocity that linearly increases via a smooth step function from 0 m/s at 0 ms to 10 m/s at 0.125 ms and remains constant thereafter. As it is being pulled from the ITZ and matrix, the fiber is prevented from rotating about the x_3 axis.

3.2. Meshing and numerical algorithm

Meshes were generated using Abaqus's native meshing algorithm [22]. Fig. 3 shows a sample meshed model for an $\varphi_e = 0.5$-mm triangular cross-section and 12.7-mm pitch fiber. The matrix was meshed by 4-node tetrahedral elements using an unstructured, graduated mesh with a characteristic element length of 380 μm at matrix faces 2–6 decreasing to a characteristic element length of 28 μm at the matrix–ITZ interface. Here, characteristic element length of a tetrahedral element is defined as the volume of a tetrahedral element divided by the maximum surface area of the four faces of the same tetrahedral element. The ITZ was meshed by 4-node linear tetrahedral elements, with a characteristic element length of 16 μm. The fiber was meshed by 8-node linear reduced integration hexahedral elements with a 110 μm seed, resulting in elements with side lengths between 94 and 111 μm. The meshing resulted in approximately 90,000 matrix elements, 14,000 ITZ elements, and 4000 fiber elements. It is noted that this numerical model is mesh sensitive. Specifically, the mesh density inherently alters the surface roughness at the fiber–ITZ interface, causing different levels of normal and surface tractions during slip. The different levels of tractions then cause varying amounts of plasticity in the matrix and the ITZ. To account for mesh-sensitivity, the model is calibrated in Section 4.

Numerical results were calculated by Abaqus/Explicit v6.10–1 running on 40 AMD 2350QC processing cores. For instantiations with $L_e = 12.5$ mm, the processing time varied from 48 to 300 h depending on the severity of contact and distortion of the ITZ and matrix elements.

4. Model calibration and validation

The model was calibrated to experimental data reported by Sujivorakul [21], who pulled twisted fibers with triangular cross sections from cement mortar with $f_c = 44$ MPa. The fibers had been embedded 12.7-mm into the cement mortar. The two data sets chosen from Sujivorakul [21] for calibration and validation had pitches of 12.7 and 38.1 mm, respectively.

In physical experiments, the free length of each fiber was minimized, leading to an unknown, yet positive distance between the face of the cementitious material and the point that the fiber was pulled from. This positive value of free length was not necessarily constant for the three fibers considered for calibration. In contrast,

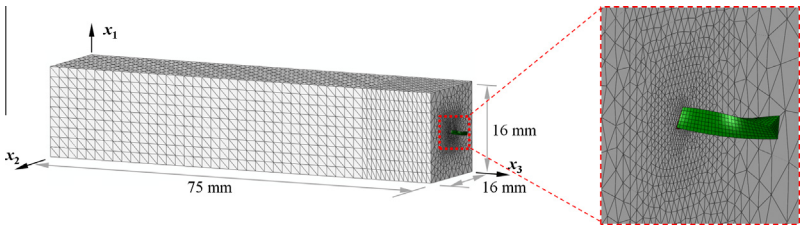

Fig. 3. Illustration of the meshed model showing the matrix (gray), ITZ (red), and fiber (green). The shown fiber has a φ_e = 0.5 mm triangular cross-section, 12.7-mm pitch, a 15.5-mm total length, and a 3.0-mm free length. (For interpretation of the references to colour in this figure legend, the reader is referred to the web version of this article.)

the numerical simulations assume a fixed free length of 3.0 mm unless specified otherwise.

The model was calibrated by adjusting the dilation angles of the matrix and the ITZ such that the pullout force as a function of end slip of the numerical simulation matched that of the aforementioned physical experiments. Here, pullout force is defined as the total traction in the positive x_3 direction on the x_3 face of the fiber (cf. Fig. 2); end slip is defined as the displacement in the x_3 direction of the x_3 face of the fiber with the reference position taken from the reference configuration. Starting with the 12.7-mm pitch fiber, dilation angles of 2° and 1° were chosen for the matrix and the ITZ. Subsequently, the model was validated by simulating a fiber–ITZ–matrix system with the same material parameters and a 38.1-mm fiber pitch. Results of the simulations generated in this work and experimental data generated by Sujivorakul [21] are compared in Fig. 4. In Fig. 4, numerical data is shown as thin dashed lines shaded red for the 12.7-mm pitch and blue for the 38.1-mm pitch. Data generated by physical experiments are shown as thick solid lines and are shaded the same color as their corresponding experimental data with the same pitch. For comparison, a third pair of curves, shaded black, indicate data for straight, smooth fibers with 0.5-mm-diameter circular cross sections. The dashed black line was generated using a numerical simulation similar to the model shown in Fig. 2, except that the fiber was straight and smooth with a 0.5-mm-diameter cross section. The mesh at the fiber–ITZ interface of the circular fiber had a characteristic element length of 55 μm, which is smaller than the characteristic element length used for the twisted triangular fibers. It is assumed that the need for the finer mesh is attributable to discretization errors introduced in three-dimensional meshing. The thick solid black line was experimentally measured in Sujivorakul [21].

Experimental and numerical results can also be compared by the maximum pullout force and the total work of pullout, defined as the integral of pullout force integrated over the end slip for end slips between zero and L_e. Fig. 5a and b compare the maximum pullout force and work during pullout for experimental data of Sujivorakul [21] and the numerical simulations utilizing the model at the single fiber length scale. In Fig. 5, data points representing experiments are shown as squares shaded red; data points representing numerical simulations are shown as circles shaded green. The two dashed lines at the bottom of each figure have a constant value, representing the value for a straight, smooth fiber. For the twisted fibers considered, the numerical simulation under-predicts the maximum pullout for by a maximum of 13%, and over-predicts the total work by 16%.

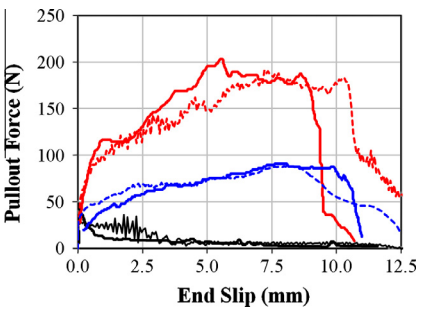

Fig. 4. Calibration and validation curves for triangular fibers with initial pitches of 12.7 (red), and 38.1 (blue) mm. The black lines represent data for straight, smooth fibers with circular cross sections. Experimental data of Sujivorakul [21] are shown as thick solid lines, and data from numerical simulations are shown as thin dashed lines. (For interpretation of the references to colour in this figure legend, the reader is referred to the web version of this article.)

4.1. Validation of elastic–plastic responses of the matrix and ITZ

Although the mechanisms in the numerical simulations cause slip-hardening and matrix tunneling, it is not assumed that the numerical model presented here provides a unique solution predicting these phenomena. In lieu of an exhaustive analysis, Fig. 6 compares the pullout forces as a function of end slip computed by the model utilizing different constitutive relations for the matrix and ITZ. The solid red curve indicates the pullout response of the elastic–plastic matrix and ITZ constitutive relations as described in Sections 2.1 and 2.2. In comparison, the dashed black line shows the pullout response of the model assuming a purely elastic response for the matrix and ITZ. At end slips less than 2 mm, the pullout responses are indistinguishable. However, for end slips between 2 and 12.5 mm, the pullout force of the model using purely elastic constitutive relations for the matrix and ITZ displays slip-softening. Additionally, the elastic curve does not display any tunneling effects as described previously.

4.2. Untwisting of fiber during pullout

Beyond reproducing the experimental pullout curves, maximum pullout force, and total work, the model reproduces the experimentally observed untwisting of fibers during pullout (cf. Kim et al. [3]). Here, untwisting is defined as the increase of a fiber's pitch from the initial pitch to a finite pitch greater than the initial pitch. To illustrate this phenomenon, Fig. 7 shows the deformation and evolution of plastic strain of the outside of a 12.7-mm initial pitch fiber at end slip increments of 2.5 mm. For clarity, the ITZ and f_c = 44 MPa matrix surrounding the fiber are not shown; however, the positive x_3 face of the cementitious matrix is marked with a light gray vertical line. At each increment of end slip, the portion of the fiber within the cementitious material is to the left of the light gray line, and is marked as the "Embedded portion of fiber". In Fig. 7, the image of the fiber at the top left of the figure represents the fiber's state of deformation and equivalent plastic strain after the matrix and ITZ have shrunk, but before the fiber has been pulled from the matrix. The image of the fiber at the bottom right represents the fiber at an end slip of 12.5 mm. At an end slip of 12.5 mm, the fiber has been removed from the matrix, but has not come to rest and may subsequently relax.

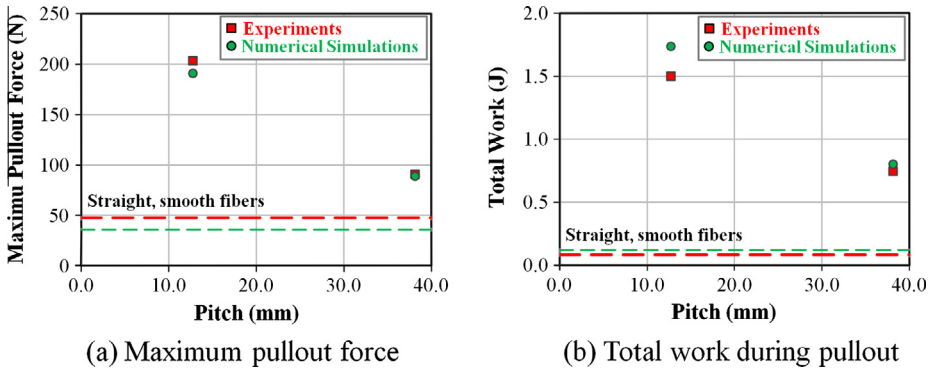

Fig. 5. (a) Maximum pullout force and (b) total work during pullout as functions of fiber pitch comparing data from experiments [21] (shaded red) and numerical simulations (shaded green) for L_e = 12.5 mm and f_c = 44 MPa. The two dashed horizontal lines at the bottom represent the value for a straight smooth fiber. (For interpretation of the references to colour in this figure legend, the reader is referred to the web version of this article.)

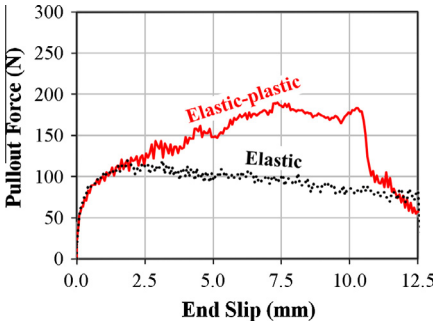

Fig. 6. Pullout force as a function of end slip for utilizing an elastic–plastic elastic ITZ–matrix (dashed black) and a elastic–plastic (solid red) ITZ–matrix system. (For interpretation of the references to colour in this figure legend, the reader is referred to the web version of this article.)

Similar to physical experiments, numerical simulations indicate that the fiber untwists due to mechanical pullout from the matrix. From Fig. 7, it is observed that equivalent plastic strain primarily accumulates in longitudinal bands positioned at the center of each of the three flats. The longitudinal bands extend from the exit of the matrix to the free tip of the fiber. From this observation, it is determined that the fiber exhibits primarily an elastic behavior within the ITZ and matrix. On the triangular fiber shown, there are three such longitudinal bands with maximum equivalent plastic strain values of 0.05.

5. Results

The results from the numerical model focus on using the numerical model to gain insights into the active mechanism of physical experiments, investigate the behavior of an in situ fiber at a crack opening distance of zero mm, and extend the model to higher unconfined compressive strength mortars containing silica fume.

5.1. Active mechanisms in the numerical model

In this section, mechanisms of the numerical model are investigated to gain insight into possible mechanisms in the physical experiments. In particular, the mechanisms of interest are the transfer of tractions from the fiber to the ITZ and matrix, causes of the slip-hardening response and tunneling response, the interplay of the different dissipation mechanisms, and extend the model to higher unconfined compresive strength mortars containing silica fume.

5.1.1. Transfer of tractions from the fiber to the ITZ and matrix

The transfer of tractions from the fiber to the ITZ and matrix can be observed in the evolution of σ_{33}, as seen in Fig. 8 for a 12.7-mm pitch fiber. For reference, Fig. 8 shows results of the same set of material properties and initial fiber geometries as the results shown in Fig. 7. Similar to Fig. 7, the ITZ and matrix surrounding the fiber have been removed for clarity and replaced with the farthest right vertical gray line marking the positive x_3 face of the matrix.

For end slips between 5.0 and 10.0 mm inclusive, there is of gradient of σ_{33} starting approximately 3 mm into the matrix and ending at the positive x_3 face of the matrix. In Fig. 8, the location of the gradient is identified as the "Stress Transition Zone (STZ)". The function of the STZ is to transfer tractions from the twisted fiber to the matrix. For example, consider the distribution of σ_{33} along

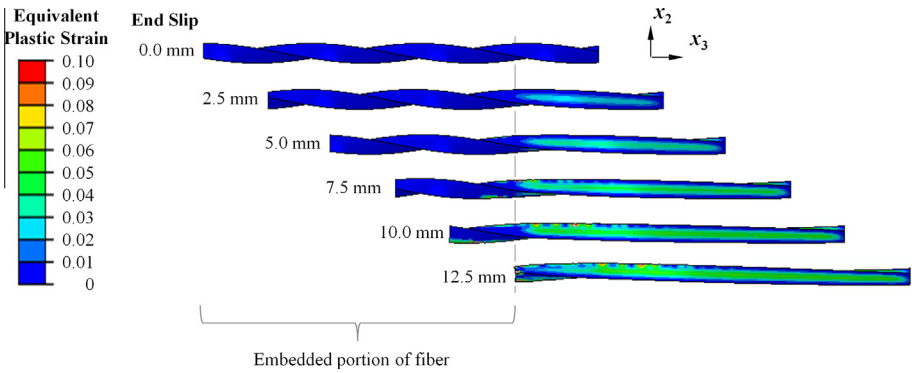

Fig. 7. Evolution of deformation and equivalent plastic strain as a function of end slip for a triangular fiber with an initial 12.7-mm pitch pulled from a f_c = 44 MPa matrix.

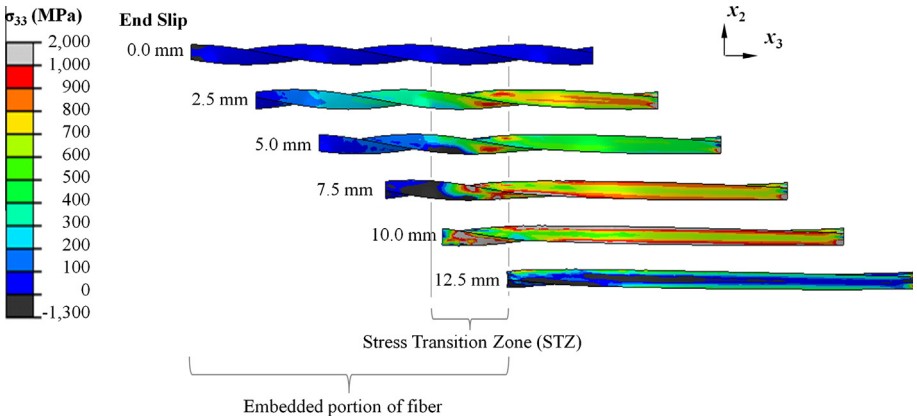

Fig. 8. Evolution of σ_{33} as a function of end slip for a triangular fiber with an initial 12.7-mm pitch pulled from a f_c = 44 MPa matrix.

the x_3 axis shown in Fig. 8 at an end slip of 5.0 mm. At the left edge, or the beginning, of the STZ, σ_{33} = 200 MPa; whereas σ_{33} = 500 MPa at the right edge, or conclusion, of the STZ. The significance of the STZ is that a small domain of material is controlling the global response of the fiber. Although similar in name, the STZ is fundamentally different than the ITZ: STZ is an inhomogeneous region composed of fiber, ITZ, and bulk matrix with a location that can only be determined only after a crack plane in the matrix has been established. The ITZ is a result of processing conditions and exists regardless of a crack plane in the cementitious materials.

5.1.2. Slip-hardening and tunneling responses

The slip-hardening and tunneling responses observed in Fig. 4 are direct consequences of the STZ. For example, Fig. 9 shows evolution of equivalent plastic strain as a function of end slip in a 12.7-mm-pitch fiber–ITZ–matrix system at a x_1 = 0 mm section view. The section view shows only a 13.5 × 5 mm^2 section of the matrix; the remainder of the matrix at this cross section had equivalent plastic strains less than 0.01.

The equivalent plastic strains within the STZ in Fig. 9 cause the numerical model to predict slip-hardening and tunneling via the following sequence of events. First, the ITZ plastically deforms via granular flow causing the matrix to dilate. The dilation of the ITZ leads to plastic deformation and dilation of the matrix within an approximate 1.25 mm radius of the fiber. This local dilation of the matrix is confined by the regions of the matrix further from the fiber, ultimately causing the normal tractions at the fiber–ITZ interface to increase. The increase in the fiber–ITZ normal tractions increase frictional resistance via the isotropic Coulomb relations, which in combination with the plasticity of the ITZ and matrix, cause the observed slip-hardening.

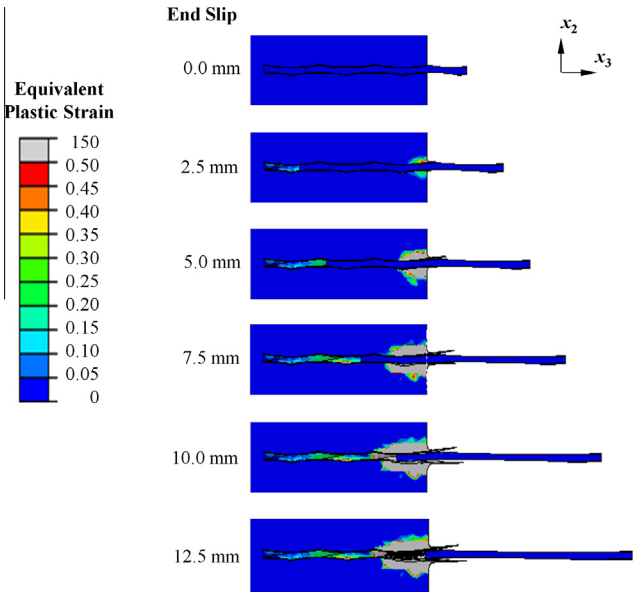

Fig. 9. Evolution of equivalent plastic strain as a function of end slip for a triangular fiber with an initial 12.7-mm pitch pulled from a f_c = 44 MPa matrix.

The tunneling response is also a consequence of granular flow of the ITZ and matrix. For example, the granular flow and dilation of the ITZ and matrix elements leads to the erosion, or displacement from the fiber bed of a small number of elements, as visible in Fig. 9 for end slip values greater than or equal to 5.0 mm. After a sufficient number of ITZ and matrix elements erode, the fiber bed surrounding the matrix no long remains in contact with the fiber, thus causing tunneling.

5.1.3. Interplay of the different dissipation mechanisms

Unlike physical experiments, numerical models allow the total work to be partitioned into different mechanisms. Fig. 10 partitions the total work into friction, plastic dissipation in the fiber–ITZ–matrix system, and strain energy for systems containing 12.7- and 38.1-mm pitch fibers. A further partitioning of the plastic dissipation portion of the energy is shown in Fig. 11, which partitions plastic dissipation in the plastic dissipation due to the granular flow of the ITZ, plastic dissipation due to plastic deformation of the fiber, and plastic dissipation due to the granular flow of the matrix material.

The energy partitions shown in Figs. 10 and 11 indicate that the model is highly dissipative, with less than 1% of the total work stored as strain energy. Of the remaining 99% of the total work, friction is the dominant energy dissipation mechanism during the first 80% of end slip. This observation is significant in that both the numerical model presented here and the analytical model presented by Sujivorakul [21] primarily account for pullout forces through frictional effects. The primary difference between the models is that the numerical model accounts for increased pullout resistance by including plasticity of the ITZ and matrix materials, instead of adding a torque component to the embedded end of the fiber.

Interestingly, plastic dissipation of the 12.7- and 38.1-mm fibers accounts for only 8% and 2% of the total work within each respective system. To explore this observation further, a numerical model was constructed of a 12.5-mm long, straight, triangular shaped fiber utilizing the same constitutive relation given in Section 2.2. The straight fiber was then twisted about its primary axis,

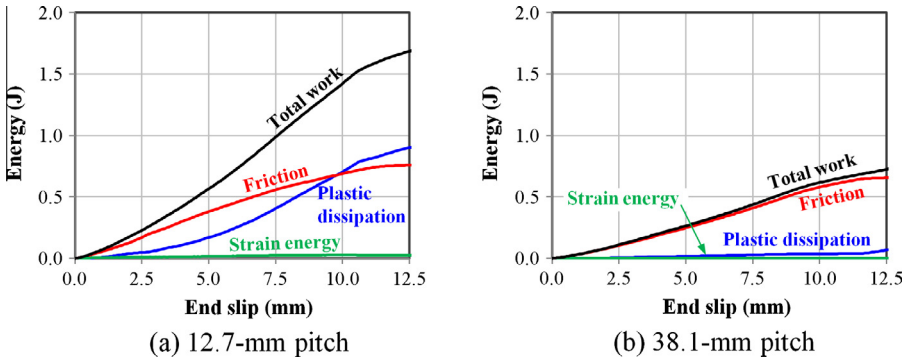

Fig. 10. Partition of total work as a function of end slip for fibers with (a) 12.7-mm and (b) 38.1-mm pitches. Each fiber was embedded 12.5 mm into an ITZ–matrix system with f_c = 44 MPa.

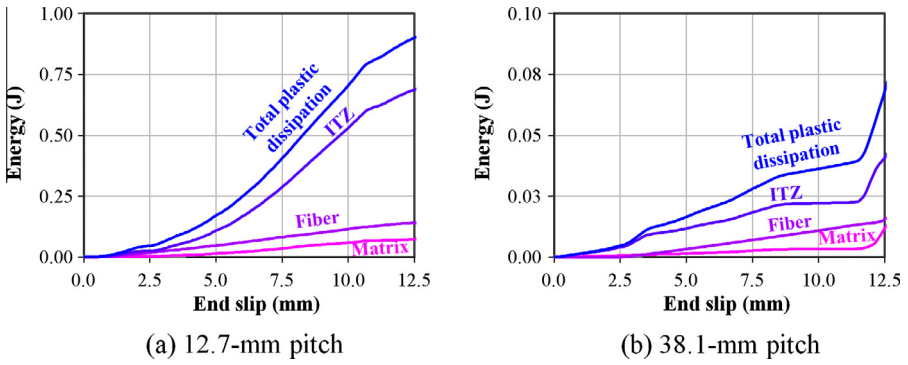

Fig. 11. Partition of total plastic dissipation as a function of end slip for (a) 12.7-mm and (b) 38.1-mm pitched fibers. Each fiber was embedded 12.5 mm into an ITZ–matrix system with f_c = 44 MPa.

i.e., the x_3 axis as shown in the Fiber Detail view of Fig. 2, in order to form twisted fibers with 12.7- and 38.1-mm pitches. The positive x_3 face of the fiber was fixed; the negative x_3 face was rotated either 8.2 or 4.9 radians, depending on whether the final pitch was 12.7 or 38.1 mm, during a smooth step function with a duration of 1 ms. During rotation, the negative x_3 face of the fiber was permitted to translate in the x_3 direction. The fiber was then allowed to relax for 1 ms before being untwisted the same number of radians as the fiber was previously twisted. Note that the angle of applied twist, i.e. 8.2 or 4.9 radians, was greater than the final desired twists of 2π or $2/3\pi$ for the 12.7- and 38.1-mm pitched fibers due to elastic recovery.

The applied torque and work required to twist the straight fibers to pitches of 12.7 and 38.1 mm are shown in Fig. 12. In Fig. 12 torque data are shown as thin dashed lines; data for the work, defined as the integral of the torque over the angle of twist, are shown as solid lines. The numerically calculated torque values

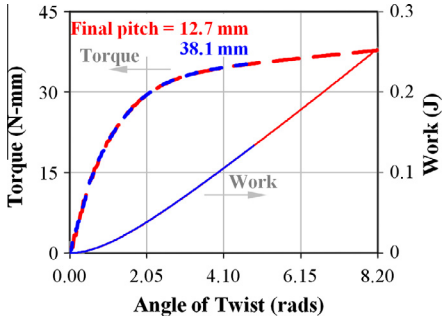

Fig. 12. Applied torque and work required to twist fibers to 12.7- and 38.1-mm pitches. Fibers have ultimate tensile strengths of 2412 MPa and lengths of 12.5 mm.

are slightly greater than the theoretical fully plastic torque value of 35 N-mm, which is calculated by

$$T_0 = \frac{2}{3}\frac{\sigma_{yield}}{\sqrt{3}}\left(\frac{b}{2}\right)^3 \tag{12}$$

as determined by Chakrabarty [32]. In the preceding equation, σ_{yield} is the yield strength of the fiber, i.e. 2,412 MPa, and b is the width of the fiber, i.e. 0.67 mm for the φ_e = 0.5 triangular shaped fiber shown in Fig. 2.

The ratio of total work required to pull a twisted fiber from a cementitious material shown in Fig. 10 to the plastic work to twist a fiber in Fig. 11 indicates that twisting polygonal fibers have a positive energy return on the work required to twist the fibers. For example, the 12.7-mm pitch fiber requires 1.72 J to be pulled from the matrix and 0.25 J to be twisted. Thus, this combination of cementitious material and fiber returns 7 times the energy for the energy required to twist the fiber.

5.2. Behavior of an in situ fiber at a crack face

Physical experiments are limited by the lack of control of all parameters. For example, the free length of the fiber can be minimized in experiments, but never eliminated. This specific limitation prevents researchers from experimentally determining the in situ behavior of twisted fibers at a crack face, where the fiber experiences a free length of 0 mm. In this section, the validated numerical model is utilized to gain insights into the pullout response at a crack face by simulating twisted fibers with zero free lengths.

Figs. 13a and b show the pullout responses of 12.7- and 38.1-mm pitch fibers comparing the pullout force versus end slip data

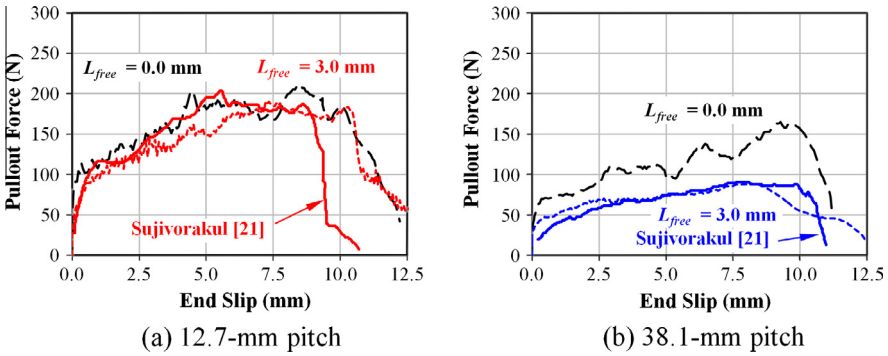

Fig. 13. The effect of free length of fiber quantified by the pullout force as a function of end slip for initial fiber pitches of (a) 12.7 mm and (b) 38.1 mm. Experimental data of Sujivorakul [21] shown as solid lines; numerical simulation data with L_{free} = 3.0 mm shaded the same color as the experimental data with dashed lines; numerical simulation data with L_{free} = 0.0 mm is shaded as black dashed lines. (For interpretation of the references to colour in this figure legend, the reader is referred to the web version of this article.)

from experiments (solid line) to those generated by numerical simulations having 3.0- and 0.0-mm free lengths.

The numerical simulations indicate that the effect of free length is more pronounced for the fiber's having larger initial pitches. In particular, the fiber with an initial pitch of 38.1 mm and L_{free} = 3.0 - mm exhibits a maximum pullout force of 90 N; whereas the same fiber–ITZ–matrix system had a maximum pullout force of 165 N. This 83% increase in pullout force is not observed in the fiber–ITZ–matrix system with 12.7-mm pitch, which shows a more modest 17% increase in maximum pullout force. The primary significance of this finding is that experimental single fiber pullout tests provide a lower bound to the pullout forces experienced in situ at a crack face.

5.3. Extended model for higher unconfined compressive strength mortar containing silica fume

For higher matrix strengths, experimental data indicates that the pullout response changes from a slip-hardening response to either a slip-neutral or slip-softening response for end slips between 10% and 80% of the fiber's embedded length. Therefore, it is expected that the previously identified STZ does not sufficiently dilate to increase the cause slip-hardening responses. Instead, the higher strength ITZs and matrices experience yielding and dilation such that either the slip-neutral or slip-softening behavior is present. For example, consider the experimental responses reported by Sujivorakul [21] shown in Fig. 14 for a 12.7-mm initial pitch fiber embedded 12.7 mm deep into two different matrices: f_c = 44 MPa and f_c = 84 MPa.

Recalling Fig. 6, the numerical model predicts slip-hardening behavior if the ITZ and matrix are assumed to have purely elastic responses. This observation motivates the modeling of fiber–ITZ–matrix systems with higher strength matrices, such as the f_c = 84 - MPa response in Fig. 14. However, changing the matrix and ITZ to elastic constitutive relations with E_m = 43.7 GPa, ν_m = 0.2, E_i = 35.0 - GPa, and ν_i = 0.2, and the linear shrinkage to −140 μm/m, per the CEB-FIB model code shrinkage estimates, under-predicts the pullout force at all end slips. A possible explanation for the under-prediction is found in the results of Chan and Chu [10], who showed cementitious material attached to straight, smooth circular fibers after being pulled from a cementitious material containing 30% silica fume by weight. The silica fume enhanced the chemical bond to the fiber, thus causing a fracture surface within the monolithically poured cementitious material. Therefore, the assumed 0.45 coefficient of friction at a steel–concrete interface is no longer valid; instead, it is assumed that the coefficient of friction increases to 1.05, which is between 1.0 for concrete placed against intentionally roughened concrete surfaces and 1.40 for concrete placed monolithically, as recommended by the American Concrete Institute's (ACI) Building Code Requirements ACI 318 [31].

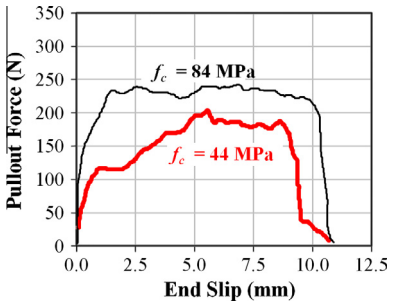

Fig. 14. Experimentally measured pullout force versus end slip displacement for fibers with an initial pitch of 12.7 mm (adapted from Sujivorakul [21]).

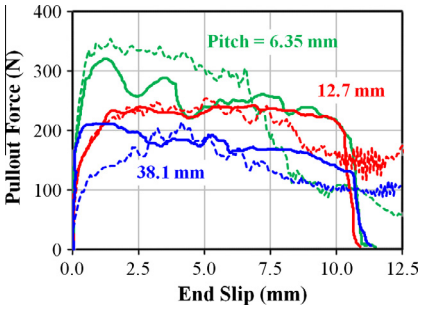

Fig. 15. Pullout force as a function of end slip for f_c = 84 MPa. Experimental data shown as solid line and numerical data shown as dashed lines.

From this assumed coefficient of friction, a simplified version of the model with elastic ITZ and matrix constitutive relations is utilized to estimate the pullout response of fibers from the matrix. The other significant change is the change to the Young's modulus brought by changes in the measured compressive strength. Fig. 15 shows the calculated pullout response from simulations as dashed lines and the measured experimental data of Sujivorakul [21] as solid lines.

A comparison of the simulated and experimental data indicate that the simulation data is in the same rank order as the experimental data. Furthermore, the maximum pullout force for each initial fiber pitch is within 10% of the maximum pullout force measured experimentally.

6. Conclusions

A 3D finite element model at the scale of a single fiber was developed to understand the active mechanisms of storage and dissipation present during the quasi-static pullout of twisted fibers from cementitious materials. The model captures physical phenomena relevant to the pullout of fibers from the concrete matrix (i.e., granular flow of the interfacial transition zone (ITZ), granular flow of the matrix, the plastic deformation of the fiber, and the friction at the interface between the fiber and the ITZ). In particular, the approach taken allows the resistance of fibers against pullout to be quantified as a function of fiber morphology, size, and properties of the fiber and matrix materials in the concrete. The model was calibrated and validated utilizing previously published experimental data for fibers having a 2400 MPa ultimate tensile strength, triangular cross sections with equivalent diameters of 0.5 mm, and pitches between 12.7 and 38.1 mm, and cementitious materials having a 44-MPa unconfined compressive strength.

Numerical simulations using the model were conducted and produced the following important findings.

- Fiber morphology can significantly influence the resistance of fibers against pullout from the cementitious material. Specifically, the twisting of fibers around their own axes can increase the maximum pullout force by 5 times and the total work during pullout by over 10 times. The mechanisms responsible for this improvement are enhanced interactions between the fiber and the ITZ caused by granular flow and dilation of the ITZ and matrix. The interactions manifest as a domain identified as the stress transition zone (STZ).
- The free length, defined as the portion of the fiber between the cementitious material and the position at which the fiber is pulled from, influences the pullout response of twisted fibers measured in physical experiments. Specifically, numerical simulations indicate that shorter free lengths, such as the free lengths found at crack surfaces in situ, cause twisted fibers to have higher pullout forces than similar fibers with longer free lengths. The level of influence varied by the fiber pitch, decreasing with decreasing fiber pitch. This finding is significant because it indicates that experimental pullout data may be viewed as conservative compared to in situ performance.
- The pullout response of twisted fibers from cementitious materials with greater unconfined compressive strengths (e.g., f_c = 84 MPa), cannot be accounted for using the same coefficient of friction values used for lower strength cementitious materials. However, numerical simulations indicate that a 1.05 coefficient of friction, which is within the 1.0 –1.4 range recommended by the American Concrete Institute for concrete to concrete surfaces, provides similar pullout responses as those found experimentally.

Acknowledgements

This work was sponsored by the Department of Homeland Security, Science and Technology Directorate, Infrastructure Protection and Disaster Management Division: Ms. Mila Kennett, Program Manager. The research was performed under the direction of Dr. Beverly P. DiPaolo, Engineer Research and Development Center (ERDC), U.S. Army Corps of Engineers (USACE). Permission to publish was granted by the Director, Geotechnical and Structures Laboratory, ERDC. Approved for public release; distribution is unlimited.

BDE gratefully acknowledges the comments provided by Dr. Beverly P. DiPaolo and the others at ERDC USACE. Furthermore, BDE acknowledges the significant quantity and quality of experimental data published by Dr. A.E. Naaman, Dr. C. Sujivorakul, and coworkers to the field of twisted fibers.

References

[1] Naaman AE, Reinhardt H, editors. Fourth international RILEM workshop on high performance fiber reinforced cement composites (HPFRCC4). Ann Arbor: RILEM Publications; 2003.
[2] Johnston CD. Fiber-reinforced cements and concretes. 1st ed. Amsterdam: Gordon and Breach Science Publishers; 2001.
[3] Kim DJ, El-Tawil S, Naaman AE. Rate-dependent tensile behavior of high performance fiber reinforced cementitious composites. Mater Struct 2009;42(3):399–414.
[4] Standard test method for flexural performance of fiber-reinforced concrete (using beam with third-point loading), ASTM, 2012.
[5] Kim DJ, Naaman AE, El-Tawil S. Comparative flexural behavior of four fiber reinforced cementitious composites. Cem Concr Comp 2008;30(10):917–28.
[6] Soroushian P, Bayasi Z. Fiber type effects on the performance of steel fiber reinforced concrete. ACI Mater J 1991;88(2):129–34.
[7] Easley TC, Faber KT, Shah SP. Use of a crack-bridging single-fiber pullout test to study steel fiber/cementitious matrix composites. J Am Ceram Soc 1999;82(12):3513–20.
[8] Boshoff WP, Mechtcherine V, van Zijl GPAG. Characterising the time-dependant behaviour on the single fibre level of SHCC: Part 2: The rate effects on fibre pull-out tests. Cem Concr Res 2009;39(9):787–97.
[9] Cunha VMCF, Barros JAO, Sena-Cruz JM. Pullout behavior of steel fibers in self-compacting concrete. J Mater Civ Eng 2010;22(1):1–9.
[10] Chan YW, Chu SH. Effect of silica fume on steel fiber bond characteristics in reactive powder concrete. Cem Concr Res 2004;34(7):1167–72.
[11] Guerrero P, Naaman AE. Effect of mortar fineness and adhesive agents on pullout response of steel fibers. ACI Mater J 2000;97(1):12–22.
[12] Focacci F, Nanni A, Bakis C. Local bond-slip relationship for FRP reinforcement in concrete. J Comp Constr 2000;4(1):24–31.
[13] Naaman AE, Namur G, Alwan JM, Najm HS. Fiber pullout and bond slip. I: Analytical study. J Struct Eng 1991;117(9):2769–90.
[14] Li CY, Mobasher B. Finite element simulations of fiber pullout toughening in fiber reinforced cement based composites. Adv Cem Based Mater 1998;7(3–4):123–32.
[15] Alwan JM, Naaman AE, Guerrero P. Effect of mechanical clamping on the pull-out response of hooked steel fibers embedded in cementitious matrices. Concr Sci Eng 1999;1:15–25.
[16] Naaman AE. Engineered steel fibers with optimal properties for reinforcement of cement composites. J Adv Concr Technol 2003;1(3):241–52.
[17] Kim D, El-Tawil S, Naaman AE. Correlation between single fiber pullout behavior and tensile response of FRC composites with high strength steel fiber. In: Reinhardt HW, editor. High performance fiber reinforced cement composites (HPFRCC5). Mainz, Germany: RILEM Publications; 2007. p. 67–76.
[18] Sujivorakul C, Naaman AE. Evaluation of bond-slip behavior of twisted wire strand steel fibers embedded in cement matrix. In: Proceedings of ACI symposium on concrete: material science to applicatioons, ACI SP-206. 2002. p. 271–292 [a Tribute to S.P. Shah].
[19] Menzel C. A proposed standard deformed bar for reinforcing concrete. In: Studies of bond between concrete and steel: a compilation of five papers. Chicago, IL: Portland Cement Association, Research and Development Laboratories; 1952. p. 11–64.
[20] Sujivorakul C, Naaman AE. Modeling bond components of deformed steel fibers in FRC composites. In: Proceedings of international workshop on high performance fiber reinforced cement composites (HPFRCC-4), RILEM Publications, 2003. p. 35–48.
[21] Sujivorakul C. Development of high performance fiber reinforced cement composites using twisted polygonal steel fibers, Ph.D. Dissertation, University of Michigan, 2002.
[22] Abaqus v6.10 Theory Manual, Dassault Systemes, 2010.
[23] Drucker DC, Prager W. Soil mechanics and plastic analysis or limit design. Quart Appl Math 1952;10:157–65.
[24] CEB-FIP, CEB-FIP Model Code 1990, Thomas Telford, 1998.
[25] Mehta P, Monteiro P. Concrete: microstructure, properties, and materials. McGraw-Hill Professional; 2005.
[26] Park SW, Xia Q, Zhou M. Dynamic behavior of concrete at high strain rates and pressures: II. Numerical simulation. Int J Impact Eng 2001;25(9):887–910.
[27] Vermeer PA, de Borst R. Non-associated plasticity for soils, concrete and rock. Heron 1984;29:1–64.
[28] Cohen MD, Lee T-FF, Goldman A. A method for estimating the dynamic moduli of cement paste-aggregate interfacial zones in mortar. In: Microstucture of cement-based systems/bonding and interface in cementitious materials, Materials research society symposium proceedings, Pittsburgh, PA, 1995. p. 407–412.
[29] Standard specification for steel wire. Music spring quality. West Conshohocken, PA: ASTM; 2007.
[30] Baltay P, Gjelsvik A. Coefficient of friction for steel on concrete at high normal stress. J Mat Civ Eng 1990;2(1):46–9.
[31] Building Code Requirements for Structural Concrete and Commentary, ACI 318-08, 2008.
[32] Chakrabarty J. Theory of plasticity. 3rd ed. Butterworth-Heinemann; 2006.